Optics Communications 481 (2021) 126543



Contents lists available at ScienceDirect

Optics Communications

journal homepage: www.elsevier.com/locate/optcom



Investigation into the thermal effects of a Nd:YVO_4 crystal at 1342 nm using the bistability-like output characteristics



Huiqi Yang [a], Jiaqi Song [a], Pixian Jin [a,b], Jing Su [a,b], Huadong Lu [a,b,*]

[a] State Key Laboratory of Quantum Optics and Quantum Optics Devices, Institute of Opto-Electronics, Shanxi University, Taiyuan 030006, China
[b] Collaborative Innovation Center of Extreme Optics, Shanxi University, Taiyuan, Shanxi 030006, China

ARTICLE INFO

Keywords:
Bistability-like output characteristics
Single-longitudinal-mode 1342/671 nm laser
Thermal loading
Energy-transfer upconversion (ETU)
Excited stimulated absorption (ESA)

ABSTRACT

The influence of energy-transfer upconversion (ETU) and excited stimulated absorption (ESA) on the thermal effects of a Nd:YVO_4 crystal was investigated in this paper. A stable continuous-wave (CW) single-frequency and intracavity frequency-doubled dual-wavelength 1342/671 nm laser was built, and the output power was manipulated by changing the transmissions of the output coupler. When the output coupler coated with a partial transmission film of 0.5% at 1342 nm was replaced by that of 8% at 1342 nm, the maximum output powers of the 671 nm and 1342 nm lasers ranged from 3.35 W and 1.08 W to 0.43 W and 6.35 W, respectively. By accurately measuring the threshold pump power as the incident pump power increased, a thermal loading of 6.8% caused by the ETU was successfully determined, which was the same for both output couplers. However, the thermal loading caused by the ESA had to be determined by measuring the threshold as the incident pump power decreased, and the measured thermal loading caused by the ESA was 14.03% for the output coupler with a transmission of 0.5%, which was larger than that of 9.13% for the transmission of 8% at 1342 nm. The measured results depicted that the thermal loadings caused by the ETU and ESA depended on the pump power and intracavity power of the 1342 nm laser, respectively. This technique for determining the thermal loadings of the Nd:YVO_4 at 1342 nm using the bistability-like output characteristics is a good method of evaluating the thermal loadings and thermal lens effects of other laser crystals.

1. Introduction

All-solid-state single-frequency continuous-wave (CW) lasers have played a major role not only in the fields of quantum information [1–3], atomic physics [4], and precision measurements [5,6], but also in the fields of pumping Ti:sap-phire lasers [7] and optical parametric oscillators (OPOs) [8,9] due to their excellent properties of perfect beam quality, high output power, and low noise, which benefited from the good performances of the laser gain materials. The advent of the Nd:YVO_4 crystal paved the way to developing a stable single-frequency laser with high output power [10] and low-intensity noise [11]. Compared to other laser crystals, the Nd:YVO_4 crystal has the advantages of a high absorption of a 808 nm laser, wide pump wavelength bandwidth, and large stimulated emission cross-sections at the $^4F_{3/2}$-$^4I_{11/2}$ and $^4F_{3/2}$-$^4I_{13/2}$ transitions, which correspond to the emissions of 1064 nm and 1342 nm lasers. To date, the output powers of single-frequency CW 1064 nm and intracavity frequency-doubled 532 nm lasers in a single resonator have achieved 101 W [12] and 30.2 W [13], respectively. In contrast to single-frequency 1064 nm and 532 nm lasers, the output powers of single-frequency 1342 nm, intracavity frequency-doubled 671 nm, and intracavity stimulated Raman scattering (SRS) lasers were restricted to 11.4 W [14], 2.8 W [15], and 250 mW [16], respectively. The quantum defect of the $^4F_{3/2}$-$^4I_{13/2}$ was larger than that of the $^4F_{3/2}$-$^4I_{11/2}$, the extra non-radiative transitions, including the excited stimulated absorption (ESA) and energy-transfer upconversion (ETU) [17], could increase the thermal loading and further increase the harmful thermal lens effect, which directly restricts the output powers of 1342 nm and 671 nm lasers and the optical conversion efficiency. Therefore, it is important to accurately measure the ETU and ESA of the Nd:YVO_4 laser crystal to scale up the output powers of 1342 nm and 671 nm lasers. In 1998, Fornasiero et al. measured the ESA of the Nd:YVO_4 crystal via a traditional method that was implemented using a CW laser as the pump beam and another light beam as the probe. The measured results revealed that the ESA of the Nd:YVO_4 crystal could seriously diminish the effective emission cross-section near a wavelength of 1342 nm [18]. In 2005, Masahito et al. estimated the heat generation of Nd-doped vanadate crystals with a 1342 nm laser action via probe light technology and confirmed that the increased thermal loading also came from the ESA by comparing the measured thermal lens lengths for lasing and non-lasing [17]. The influence of

* Corresponding author at: State Key Laboratory of Quantum Optics and Quantum Optics Devices, Institute of Opto-Electronics, Shanxi University, Taiyuan 030006, China.
E-mail address: luhuadong@sxu.edu.cn (H.D. Lu).

https://doi.org/10.1016/j.optcom.2020.126543
Received 22 July 2020; Received in revised form 16 October 2020; Accepted 17 October 2020
Available online 20 October 2020
0030-4018/© 2020 Elsevier B.V. All rights reserved.

the ETU on the laser's efficiency at an emitting wavelength of 1342 nm was derived by Chen et al. in 2000. They developed an analytical model to study the influence of the gain medium's doping concentration on the performance of the 1342 nm laser and showed that the ETU could dramatically reduce the upper-state population and decrease laser's the optical efficiency [19]. In 2018, Ma et al. presented a self-consistent theoretical model to guide the design of a 1342 nm laser by considering the ETU and ESA [20]. In 2019, Shen et al. further improved probe light technology by measuring the probe beam's divergence for lasing and non-lasing cases and presented an optimized multi-segmented crystal that displayed lower thermal lens dioptric power and more homogeneous pump distribution than conventional crystals [21]. However, to the best of our knowledge, there is no effective and simple method to accurately determine the ETU and ESA effects of the Nd:YVO_4 crystal at 1342 nm. The influence of the ETU and ESA of laser crystals can also be presented as the waste heat. Conversely, the ETU and ESA of crystals can be accurately determined using the laser's output characteristics. In this study, we developed an effective method of accurately measuring the whole thermal loading and thermal loadings caused by the ETU and ESA of a Nd:YVO_4 crystal of a 1342 nm laser using the bistability-like output characteristics that could be implemented by recording the output power trends of single-frequency CW dual-wavelength 1342 nm and 671 nm lasers.

2. Experimental design and results

To investigate the thermal effects using the bistability-like output characteristics of an active laser medium, we built a conventional LD-pumped CW single-longitudinal-mode (SLM) 1342/671 nm dual-wavelength laser, which is shown in Fig. 1. The pump source used in the experiment was a commercial fiber-coupled laser diode (LD, M1F4S22-880-50C, Dilas Co., Ltd.) with a center wavelength and maximal emitting power of 878.6 nm and 60 W, respectively. The power was manipulated by controlling the LD current that was installed in a homemade laser controller (LC) (LC, DSP-I Laser System Controller, YuGuang Co., Ltd.) with a current and temperature precision of 0.01 A and 0.01°, respectively. The fiber's core diameter and number aperture (NA) were 400 μm and 0.22, respectively. The LD's output beam was focused at the center of the gain medium by a telescope system consisting of two lenses with the focal lengths of 30 mm (f_1) and 80 mm (f_2). The spot radius of the pump light imaged on the laser crystal was approximately 510 μm. The resonator was a figure-eight-shaped ring cavity constructed using four mirrors (M_1-M_4). The input coupler M_1 was a concave–convex mirror with a curvature radius of 1500 mm (R = −1500 mm) that was coated with high-reflection (HR) film at 1342 nm ($R_{1342\ nm} > 99.5\%$) and high-transmission (HT) film at 880 nm ($T_{880\ nm} > 95\%$). M_2 was a plane-convex mirror with a curvature radius of 1500 mm (R = −1500 mm) that was coated with HR film at 1342 nm ($R_{1342\ nm} > 99.5\%$) and HT film at 1064 nm ($T_{1064\ nm} > 97\%$). M_3 and M_4 were plane-concave mirrors with a curvature radius of 100 mm (R = 100 mm). M_3 was also coated with HR film at 1342 nm ($R_{1342\ nm} > 99.5\%$) and HT film at 1064 nm ($T_{1064\ nm} > 99\%$). M_4 was an output coupler coated with partial transmission film at 1342 nm and HT film at 671 nm ($T_{671\ nm} > 95\%$).

The gain medium was an a-cut composite YVO_4/Nd:YVO_4 (yttrium vanadate/Nd^{3+}-doped yttrium vanadate) crystal with a length of 20 mm (including an undoped end cap of 5 mm and a 0.3% Nd^{3+}-doped yttrium vanadate of 15 mm) and a wedge angle of 1.5° at the second end face. Both of the crystal's end-faces were coated with anti-reflective (AR) films at 1342 nm, 1064 nm, and 880 nm. Due to the Nd:YVO4 crystal's high birefringent properties, the wedge crystal acted as a polarizing beam splitter to suppress unwanted σ polarization oscillation and enhance the superiority of the π polarization oscillation in a ring resonator [22]. The AR film at 1064 nm coated on the gain medium and mirrors (M_2 and M_3) effectively suppressed the oscillation of the 1064 nm laser [20]. The gain medium's c-axis was parallel to the laser

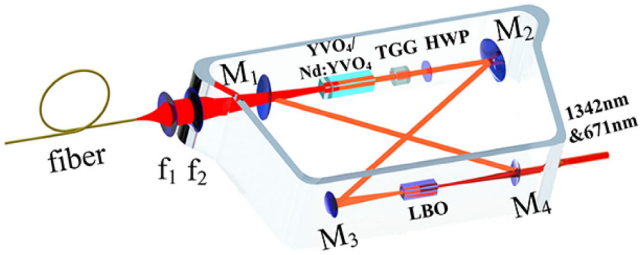


Fig. 1. Schematic diagram of the LD-pumped CW SLM dual-wavelength 1342 nm and 671 nm Nd:YVO_4 laser.

resonator's tangential plane to realize the mutual astigmatism compensation between the gain medium's thermal lens and the resonator, including four off-axis cavity mirrors that eliminated the influence of the Nd:YVO_4's thermal lens astigmatism as much as possible [22]. An optical diode consisting of an 8 mm cylindrical terbium gallium garnet (TGG) surrounded by a permanent magnet and a zero-order half-wave plate (HWP) was inserted into the resonator to ensure the laser's unidirectional oscillation. A type-I critical phase-matching LBO crystal coated with AR films at 1342 nm and 671 nm on both end faces (3 mm × 3 mm × 23 mm) was placed at the beam waist between the M_3 and M_4 mirrors to ensure the SLM operation and implement the laser's dual-wavelength output. The laser's longitudinal-mode structure was monitored by a scanned Fabry–Perot cavity (F-P-100, Yuguang Co., Ltd.) with a free spectral range of 750 MHz and a finesse of 120.

To improve the measurement precision, two output couplers coated with $T_{1342\ nm} = 0.5\%$ and $T_{1342\ nm} = 8\%$ were used to generate typical 671 nm and 1342 nm lasers, respectively. The output powers of 1342 nm and 671 nm lasers were recorded by two power meters (PM30, Coherent Co., Ltd.), respectively. When the output coupler was coated with a partial transmission film at 1342 nm ($T_{1342\ nm} = 0.5\%$) and an HT film at 671 nm and the laser's resonator length was precisely matched, the output powers of the 1342 nm and 671 nm lasers were recorded as illustrated in Fig. 2. When the LD's absorbed pump power was continuously increased, there was no laser when the absorbed pump power was up to 40.53 W. At this time, the 671 nm laser suddenly appeared with the 1342 nm laser, and the output powers of the 671 nm and 1342 nm lasers reached 2.33 W and 1.04 W, respectively. As the pump power further increased, the output power of the 671 nm and 1342 nm lasers slowly decreased due to the severe thermal lens effect and deviations from optimal mode matching. Conversely, as the LD's pump power continuously decreased, the output powers of the 671 nm and 1342 nm lasers increased instead of decreasing, and the maximal output power of the 671 nm laser could reach 3.35 W, which to the best of our knowledge was the highest output power of the intracavity frequency-doubled 1342 nm laser. In this case, the laser worked with stable SLM operation by scanning the F–P cavity. The F–P cavity's transmission curve is depicted in Fig. 3. The transverse-mode structures of the 671 nm and 1342 nm lasers were also measured with an M^2 meter. The results are illustrated in Figs. 4 and 5. The measured beam qualities of the 671 nm and 1342 nm lasers were $M_x^2 = 1.17$ and $M_y^2 = 1.17$ and $M_x^2 = 1.07$ and $M_y^2 = 1.06$, respectively. The power stability of the 671 nm laser was also measured, and the measured stability was better than ±1.5%, which is depicted in Fig. 6. As the absorbed pump power decreased to 35.96 W, the generated 671 nm and 1342 nm lasers simultaneously disappeared. As shown in Fig. 2, it was easy to ascertain the bistability-like output characteristics that resulted from the contributions of the quantum defect, ETU, and ESA.

For comparison, when the output coupler was replaced by another coupler coated with 8% transmission film at 1342 nm and HT film at 671 nm, the output powers of the single-frequency 671 nm and 1342 nm lasers versus the absorbed pump power were also recorded,

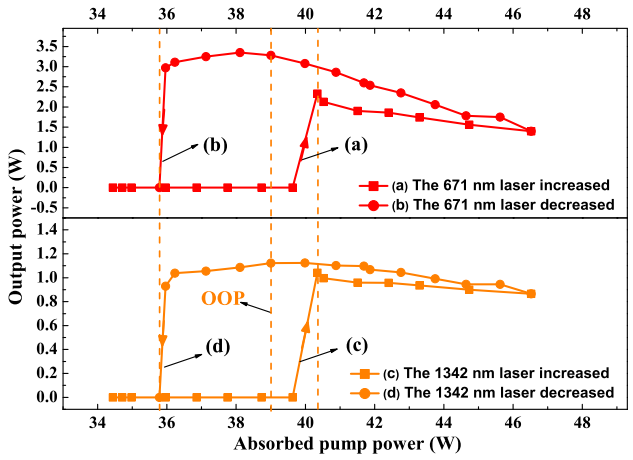


Fig. 2. Output powers of the 1342 nm and 671 nm lasers as a function of the absorbed pump power at T = 0.5%. OOP, optimal operating point.

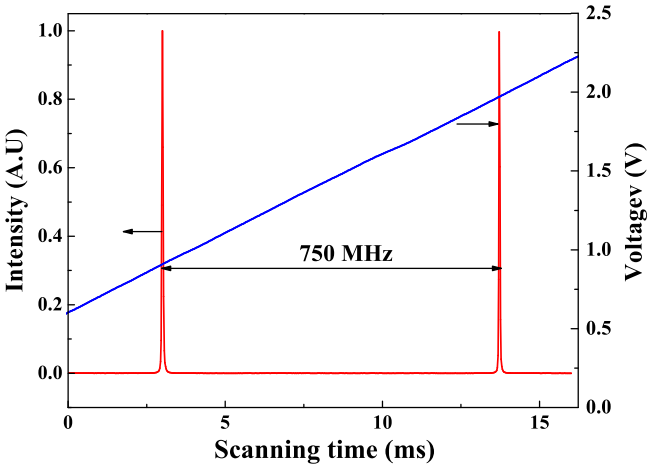


Fig. 3. Longitudinal-mode structure of the 1342 nm laser.

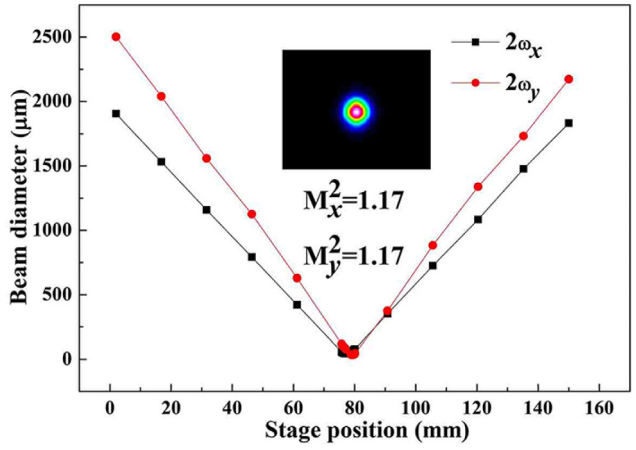


Fig. 4. Beam quality M^2 of the 671 nm laser.

which are shown in Fig. 7. In this case, the output power of the single-frequency 1342 nm laser was up to 6.35 W, far higher than that of the 671 nm laser (0.8 W). As demonstrated in Fig. 7, the threshold absorbed pump power was 40.7 W. Although the bistability-like characteristic of the laser was still observed, the separation of the output power trends as the pump power increased and decreased narrowed significantly. As shown in Figs. 2 and 7, manipulating the 1342 nm laser's intracavity power by changing the output coupler's transmission effectively controlled the output characteristics of the designed single-frequency dual-wavelength 671 nm and 1342 nm lasers. However, there was no effect on the laser's threshold pump power.

3. Investigation of the thermal effects of the Nd:YVO_4 crystal

As shown in Figs. 2 and 7, the bistability-like output characteristics of the Nd:YVO_4 laser at a wavelength of 1342 nm indicated that the laser's stability range and the Nd:YVO_4 crystal's thermal effects differed as the incident pump power increased and decreased. The laser's output characteristics were related to the laser resonator's stability range, which was influenced by the optical elements' thermal lens effects. Therefore, it was completely feasible that the gain crystal's thermal lens and thermal loading could be investigated and determined using the laser system's output characteristics. When the laser resonator's tangential and sagittal planes were simultaneously satisfied the condition of stability ranges, the 1342 nm laser began to oscillate in the resonator. In this case, the laser crystal's thermal focal length was easily measured by recording the threshold pump power. The thermal loading ξ was also determined using the measured thermal focal length. The relationship between the thermal lens effect and laser resonator's stability ranges using the ABCD matrixes is analyzed in Appendix.

Below the threshold, the ESA could be ignored because there was no corresponding energy level for the ESA effect at pump wavelengths of 808 nm, 888 nm and 914 nm in the Nd:YVO_4 crystal according to the calculated upper ESA energy levels and corresponding manifolds [23]. In this case, the Nd:YVO_4's thermal loading ($\xi_{non-lasing}$) was mostly ascribed to the quantum defect ($1-\frac{\lambda_p}{\lambda_f}$) and ETU ($\xi_{ETU}$). The ETU was an energy-transfer process converting two neighboring excited ions at the upper laser level into one excited ion, which could reduce the active particle population of the upper laser level and further aggravate the thermal loading. The fractional reduction in the population inversion due to the ETU was expressed as the ETU's thermal loading, that is, ξ_{ETU} [24]. The thermal loading below the threshold can be expressed as [25]:

$$\xi_{non-lasing} = (1-\xi_{ETU})(1-\frac{\lambda_p}{\lambda_f}) + \xi_{ETU} \quad (1)$$

where ($1-\xi_{ETU}$) is the fraction of the upper inversion ions that cause the quantum defect, λ_p is the pump laser wavelength, and λ_f is the Nd:YVO_4 crystal's average fluorescence wavelength at 1032 nm [24]. As shown in Eq. (1), the ξ_{ETU} can be expressed as:

$$\xi_{ETU} = \frac{\lambda_f}{\lambda_p}[\xi_{non-lasing} - (1-\frac{\lambda_p}{\lambda_f})] \quad (2)$$

Once the pump power was beyond the threshold, the oscillation of the 1342 nm laser rapidly built, and the pump power mainly transformed into the power of the 1342 nm laser because the energy transition occurred between the specific energy levels $^4F_{3/2}$-$^4I_{13/2}$. Different from the thermal loading before the laser generation, the ESA had to be taken into account when the 1342 nm laser began to oscillate in the resonator, as there were corresponding energy levels for doped ions to implement the transitions after absorbing the generated 1342 nm laser, and the absorption cross-section of the 1342 nm laser was up to one-tenth of the stimulated emission cross-section [17,26]. In contrast, the thermal loading caused by the ETU was too small to be considered because the population inversion above the threshold was sharply reduced due to the high power output of the 1342 nm laser (the average population almost decreased to one-tenth, which decreased from 1.99×10^{16} m^{-3} to 2.50×10^{15} m^{-3} at T = 8% at 1342 nm and 1.55×10^{15} m^{-3} at T = 0.5% at 1342 nm. Following our theoretical predictions, we further obtained ξ_{ETU} = 1.84% at T = 8% at 1342 nm and ξ_{ETU} = 0.66% at T = 0.5% at 1342 nm, which was small enough to ignore compared with the whole thermal loading). Therefore, the

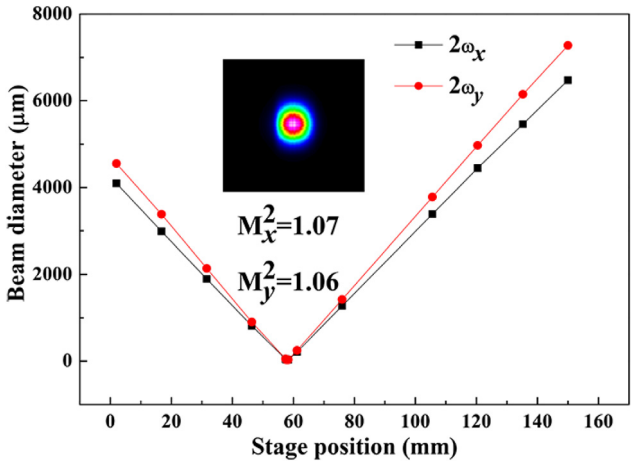


Fig. 5. Beam quality M^2 of the 1342 nm laser.

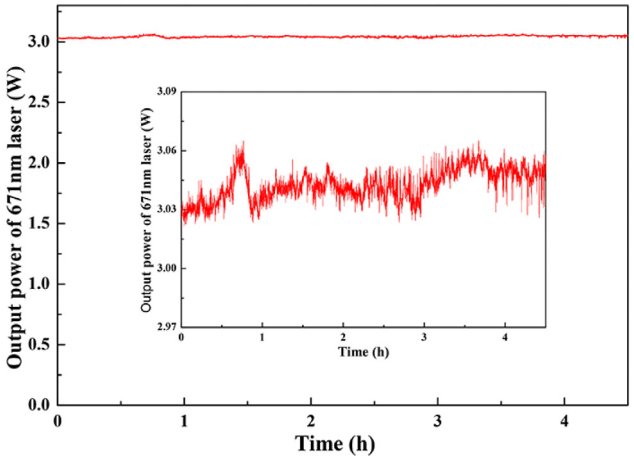


Fig. 6. Long-term stability of the 671 nm laser.

thermal loadings above the laser threshold could be ascribed to the contributions of the quantum defect and ESA. Thus, the thermal loading beyond the threshold can be expressed as:

$$\xi_{lasing} = (1 - \xi_{ESA})(1 - \frac{\lambda_p}{\lambda_l}) + \xi_{ESA} \tag{3}$$

where $(1 - \xi_{ESA})$ is the fraction of the upper inversion ions that cause the quantum defect and λ_p and λ_l are the wavelengths of the pump and fundamental laser, respectively. Thus, the ξ_{ESA} after generating of the laser can easily be expressed as:

$$\xi_{ESA} = \frac{\lambda_l}{\lambda_p}[\xi_{lasing} - (1 - \frac{\lambda_p}{\lambda_l})]. \tag{4}$$

4. Determining the results of the ETU and ESA

In the experiment, a threshold pump power of 40.53 W was attained as shown in Fig. 2 when an output coupler with a transmission of 0.5% at 1342 nm was employed, which was approximately the same as 40.7 W, as demonstrated in Fig. 7 when the output coupler was replaced by another coated coupler with a transmission of 8% at 1342 nm. The results showed that the critical points of the laser resonator's stability ranges were almost the same, which to a great extent depended on the laser crystal's thermal lens effect. According to the condition of stability ranges presented in the Appendix, the laser was emitted when the Nd:YVO_4 crystal's thermal focal lengths were 171.35 mm in the tangential plane and 130.21 mm in the sagittal plane. The whole

Table 1
Parameters of the laser.

Parameters	φ (°)	$K_{\perp c}$ (W/m/K)	$K_{\parallel c}$ (W/m/K)	ω_p (mm)	$\frac{dn}{dT}$ ($\times 10^{-6}$/K)	α (cm^{-1})	l (mm)
Value	10	5.1	5.23	0.51	3	1.5	15

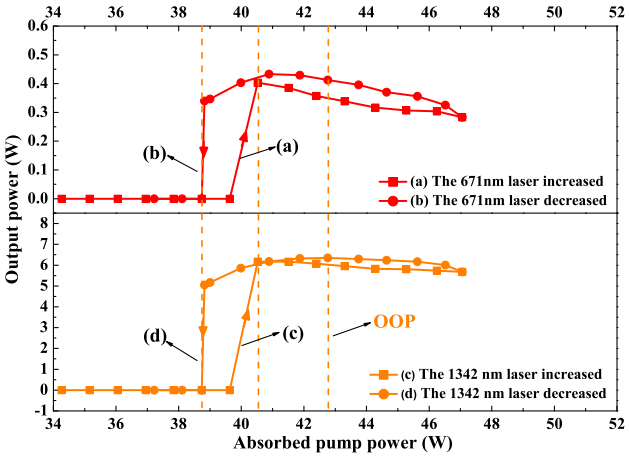


Fig. 7. Output powers of the 1342 nm and 671 nm lasers as a function of the absorbed pump power at T = 8%. OOP, optimal operating point.

thermal loading of $\xi_{non-lasing}$ = 20.5% caused by the ETU and quantum defect at the threshold was obtained by substituting the measured threshold, the parameters listed in Table 1, and the Nd:YVO_4 crystal's attained thermal lens into Eqs. (10) and (11) in Appendix. The whole thermal loading of $\xi_{non-lasing}$ = 20.5% caused by the ETU and quantum defect at the threshold was obtained. And the thermal loading of 6.8% caused by ETU (ξ_{ETU}) at the threshold was successfully attained using Eq. (2). The results showed that the thermal loading of 6.8% caused by the ETU at the threshold was approximately one-third of the whole thermal loading. Thus, the ξ_{ETU} was too large to ignore when the Nd:YVO_4 crystal was employed to launch the 1342 nm laser beam.

As shown in Fig. 2, as the pump power decreased, the 1342 nm laser oscillated until the absorbed pump power was as low as 35.96 W. The new measured threshold of 35.96 W differed from that of 40.53 W as the pump power increased, which was due to the bistability-like output characteristics. The Nd:YVO_4 crystal's thermal lenses of could be determined using the condition of stability ranges presented in Appendix. The laser continued oscillating when the Nd:YVO_4 crystal's thermal focal lengths were 68.96 mm in the sagittal plane and 90.75 mm in the tangential plane. The whole thermal loading of ξ_{lasing} = 43.63% was obtained using the newly attained thermal focal length. By substituting the newly attained whole thermal loading into Eq. (4), the thermal loading of ξ_{ESA} = 14.03% was obtained at $T_{1342\ nm}$ = 0.5% and SHG conversion efficiency of 1.60%. Similarly, when the output coupler coated with a transmission of 8% in the 1342 nm laser was utilized, the new threshold pump power of 38.83 W with an SHG conversion efficiency of 0.54% was achieved by decreasing the pump power as shown in Fig. 7. In this case, the Nd:YVO_4 crystal's thermal focal lengths were 68.94 mm in the sagittal plane and 90.74 mm in the tangential plane. The whole thermal loading and thermal loading caused by the ESA were ξ_{lasing} = 40.41% and ξ_{ESA} = 9.13%, respectively. The results attained depicted that the higher the output coupler's transmission, the smaller the ξ_{lasing} and ξ_{ESA}. In other words, the thermal lens, ξ_{lasing} and ξ_{ESA} could be effectively manipulated by changing the intracavity power of the 1342 nm laser by adopting output couplers with different transmissions and changing corresponding SHG conversion efficiency.

The thermal lenses, ξ_{lasing}, and ξ_{ESA} could also be determined using the optimal operating point (OOP) as illustrated in Figs. 2 and 7. The OOP represented the laser's operation state when the laser beam size in

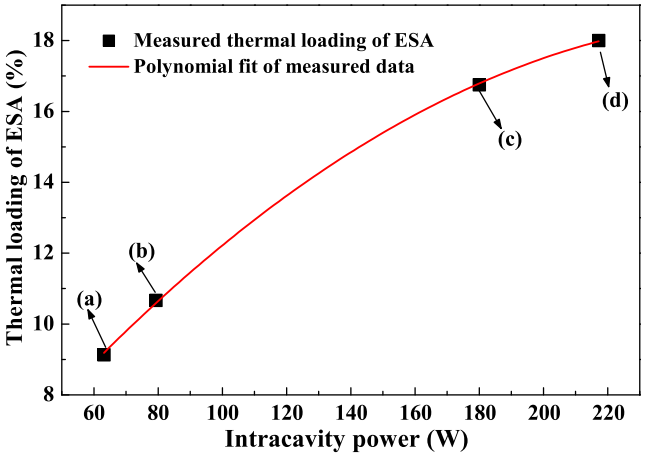


Fig. 8. Thermal loading caused by the ESA with lasing versus the intracavity power at 1342 nm. (a) The thermal loading of ESA operating at the threshold when T = 8%. (b) The thermal loading of ESA operating at the optimal operating point when T = 8%. (c) The thermal loading of ESA operating at the threshold when T = 0.5%. (d) The thermal loading of ESA operating at the optimal operating point when T = 0.5%.

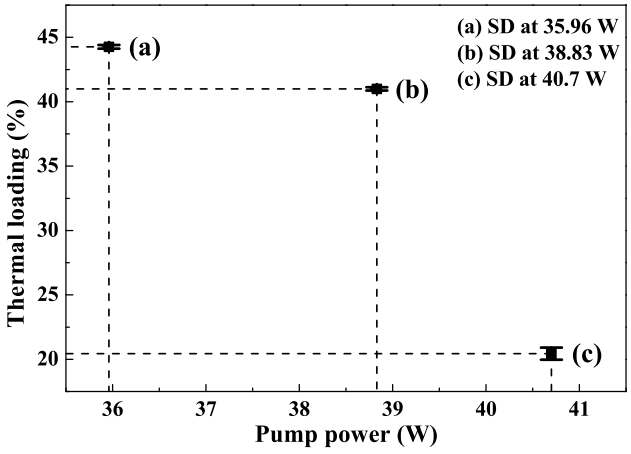


Fig. 9. Measured thermal loadings and corresponding standard deviations (SD).

the laser crystal in the tangential plane was the same as in the sagittal plane [27], which meant that the optimal mode matching between the pump and laser beams was achieved. In this case, the laser could work with stable SLM operation, and the output power of 1342 nm laser was the highest. The OOPs are denoted in Figs. 2 and 7. They were 39.00 W and 42.76 W in the output couplers at $T_{1342\ nm}$ = 0.5% and $T_{1342\ nm}$ = 8%, respectively. At $T_{1342\ nm}$ = 0.5% and SHG conversion efficiency of 1.46%, the determined thermal focal lengths of the Nd:YVO_4 crystal were 80.40 mm and 61.09 mm in the tangential and sagittal planes, respectively. The ξ_{lasing} and ξ_{ESA} values were 45.41% and 16.75%, respectively. At $T_{1342\ nm}$ = 8% and SHG conversion efficiency of 0.52%, the determined thermal focal lengths were 80.40 mm and 61.09 mm in the tangential and sagittal planes, respectively. Using the thermal focal lengths, the ξ_{lasing} and ξ_{ESA} were determined as 41.42% and 10.67%, respectively. The relationship between the ξ_{ESA} and the 1342 nm laser's intracavity power according to the transmission of the output coupler and output power is depicted in Fig. 8. The ξ_{ESA} value increased as the 1342 nm laser's intracavity power increased.

Regarding the measurement method's accuracy, the error was mainly caused by the estimation of the resonator length. Fig. 9 shows that the 1 mm error in determining the resonator length led to a standard deviation of 0.4654 in determining the laser crystal's whole thermal loading at the thresholds as the pump power increased at $T_{1342\ nm}$ = 0.5% and $T_{1342\ nm}$ = 8% and led to standard deviations of 0.1415 and 0.1306 in determining the whole thermal loading at the thresholds as the pump power decreased at $T_{1342\ nm}$ = 0.5% and $T_{1342\ nm}$ = 8%, respectively.

5. Conclusion

In summary, we developed a simple method of determining the thermal lens effect of a laser crystal and the thermal loadings caused by the ETU and ESA using the bistability-like output characteristics of stable single-frequency dual-wavelength 1342/671 nm laser. In the experiment, by increasing the incident pump power to measure the threshold, the thermal loading caused by the ETU of 6.8% at the threshold was first determined. There was almost no difference at different output coupler transmissions. The thermal loading caused by the ESA was determined by decreasing the incident pump power to measure the new threshold. At T = 0.5% and an SHG conversion efficiency of 1.60%, the thermal loading caused by the ESA was 14.03%, which differed from 9.13% at T = 8% and an SHG conversion efficiency of 0.54%. The thermal loading caused by the ESA was also determined using the OOP. Using these results, we further concluded that in addition to the quantum defect, the thermal loading before lasing mainly came from the ETU effect. However, the ETU effect became small enough to neglect once the 1342 nm laser began to oscillate, and the thermal loadings mainly came from the ESA effect and quantum defect. Moreover, the ξ_{ESA} was effectively manipulated by changing the intracavity laser power at 1342 nm by adopting output couplers with varying transmissions and changing the corresponding SHG conversion efficiency. The determined ETU and ESA could provide a good reference to scale up the output powers of the CW single-frequency 1342 nm and 671 nm lasers. Meanwhile, our study provides a good method of estimating the thermal lens effect and thermal loading of other laser crystals, which can be used to develop various types of high-performing lasers.

Declaration of competing interest

The authors declare that they have no known competing financial interests or personal relationships that could have appeared to influence the work reported in this paper.

Funding

This study was supported by the National Natural Science Foundation of China (61975100); the Key R&D Program of Shanxi Province (201903D111001); the Fund for Shanxi "1331 Project" Key Subjects Construction.

Appendix

The ABCD matrixes of the laser cavity in the tangential and sagittal planes were respectively expressed in detail as (taking the gain crystal as the starting point):

$$\begin{bmatrix} A_s & B_s \\ C_s & D_s \end{bmatrix} = \begin{bmatrix} 1 & l_{1th} \\ 0 & 1 \end{bmatrix} \begin{bmatrix} 1 & 0 \\ \frac{-2}{\rho_1} cos\varphi & 1 \end{bmatrix} \begin{bmatrix} 1 & l_{41} \\ 0 & 1 \end{bmatrix} \begin{bmatrix} 1 & 0 \\ \frac{-2}{\rho_2} cos\varphi & 1 \end{bmatrix} \begin{bmatrix} 1 & l_{3lbo} + \frac{l_{lbo}}{n_{lbo}} + l_{lbo4} \\ 0 & 1 \end{bmatrix} \begin{bmatrix} 1 & 0 \\ \frac{-2}{\rho_2} cos\varphi & 1 \end{bmatrix} \begin{bmatrix} 1 & l_{23} \\ 0 & 1 \end{bmatrix} \begin{bmatrix} 1 & 0 \\ \frac{-2}{\rho_1} cos\varphi & 1 \end{bmatrix} \begin{bmatrix} 1 & l_{th2} \\ 0 & 1 \end{bmatrix} \begin{bmatrix} 1 & 0 \\ \frac{-1}{f_{s(thermal)}} & 1 \end{bmatrix} \quad (5)$$

$$\begin{bmatrix} A_t & B_t \\ C_t & D_t \end{bmatrix} = \begin{bmatrix} 1 & l_{1th} \\ 0 & 1 \end{bmatrix} \begin{bmatrix} 1 & 0 \\ \frac{-2}{\rho_1} sec\varphi & 1 \end{bmatrix} \begin{bmatrix} 1 & l_{41} \\ 0 & 1 \end{bmatrix} \begin{bmatrix} 1 & 0 \\ \frac{-2}{\rho_2} sec\varphi & 1 \end{bmatrix} \begin{bmatrix} 1 & l_{3lbo} + \frac{l_{lbo}}{n_{lbo}} + l_{lbo4} \\ 0 & 1 \end{bmatrix} \begin{bmatrix} 1 & 0 \\ \frac{-2}{\rho_2} sec\varphi & 1 \end{bmatrix} \begin{bmatrix} 1 & l_{23} \\ 0 & 1 \end{bmatrix} \begin{bmatrix} 1 & 0 \\ \frac{-2}{\rho_1} sec\varphi & 1 \end{bmatrix} \begin{bmatrix} 1 & l_{th2} \\ 0 & 1 \end{bmatrix} \begin{bmatrix} 1 & 0 \\ \frac{-1}{f_{t(thermal)}} & 1 \end{bmatrix} \tag{6}$$

The laser's stability ranges can be expressed as:

$$|A_t + D_t| \le 2 \;\&\; |A_s + D_s| \le 2 \tag{7}$$

The laser's optimal operating point can be expressed as [27]:

$$\sqrt{\frac{2\lambda_l |B_t|}{\pi\sqrt{4-(A_t+D_t)^2}}} = \sqrt{\frac{2\lambda_l |B_s|}{\pi\sqrt{4-(A_s+D_s)^2}}} \tag{8}$$

where A_t and D_t are the corresponding ABCD matrix parameters in the tangential plane, and A_s and D_s are the corresponding ABCD matrix parameters in the sagittal planes. ρ_1 and ρ_2 are the curvature radii of spherical mirrors $M_{1,2}$ and $M_{3,4}$, respectively. φ is the incident angle of the generated laser. $l_{i,j}$ (i and j represent M_1, M_2, M_3, M_4, thermal lens at gain medium, or LBO, respectively) is the distance between i and j. The distance between M_1 and M_2 is $l_{1th}+l_{th2}$. l_{lbo} and n_{lbo} are the length and refractive index of LBO, respectively. Some listed parameters of these matrixes were known for an established stable cavity, including the resonator optical length, curvature radii, incident angles of the cavity mirrors, and the parameters of the laser and nonlinear crystals (Nd:YVO_4 and LBO), except for the pump power and thermal loading parameters. In this experiment, the distance between M_3 and M_4 was approximately 96.8 mm, and the total length of the laser path was approximately 531.92 mm.

The equivalent thermal lens focal length of a gain crystal with a Gaussian pump can be expressed as [22,28]:

$$f_{thermal} = \frac{\pi K \omega_p^2}{\xi P_{abs} \chi} \tag{9}$$

where K is the thermal conductivity coefficient. ω_p is the spot radius of the pump light imaged on the laser crystal. ξ is the thermal loading. P_{abs} is the absorbed pump power, whose value equals to $P_p \times [1 - \exp(-\alpha l)]$. P_p is the incident pump power. $1 - \exp(-\alpha l)$ is the absorption efficiency. α and l are the absorption coefficient and geometric length of the laser crystal's doped portion, respectively. χ is an effective thermo-optical coefficient including the temperature-dependent refractive index (dn/dT), surface end bulging index and stress-induced photoelastic refractive index. In the composite anisotropic uniaxial Nd: YVO_4 crystal, the thermo-optical effects caused by the surface end bulging can be neglected as the non-doped crystal on the doped laser crystal functions as a heat sink for the pumping surface and can markedly restrain the thermal deformation [29]. However, the photoelastic effect must be considered because it can cause differences in the refractive index in the directions parallel and perpendicular to the optical axis, which can directly introduce thermal aberrations in the fundamental laser at the gain crystal. The equivalent thermal lens focal lengths of the gain crystal in the tangential and sagittal planes with a Gaussian pump can be expressed separately as [15,21,22,28]:

$$f_{t(thermal)} = \frac{\pi K_{\|c} \omega_p^2}{\xi P_{abs} \frac{dn}{dT}} \tag{10}$$

and

$$f_{s(thermal)} = \frac{\pi K_{\perp c} \omega_p^2}{\xi P_{abs} (\frac{dn}{dT} + 0.85 \times 10^{-6})} \tag{11}$$

where $K_{\|c}$ and $K_{\perp c}$ are the thermal conductivity coefficients in the directions parallel and perpendicular to the optical axis, respectively. In addition to the astigmatism of the laser crystal, off-axis spherical mirrors of the ring resonator can also introduce the astigmatism because the focusing parameters of the reflected beams in the tangential plane differ from those in the sagittal plane. Both can be expressed respectively as:

$$f_t = \frac{\rho cos\varphi}{2} \tag{12}$$

and

$$f_s = \frac{\rho sec\varphi}{2} \tag{13}$$

In this experiment, to achieve a stable and efficient single-frequency laser, the astigmatism caused by the gain medium's thermal lens effect must be well compensated by that of the ring resonator's off-axis spherical mirrors.

References

[1] M.R. Huo, J.L. Qin, J.L. Cheng, Z.H. Yan, Z.Z. Qin, X.L. Su, X.J. Jia, C.D. Xie, K.C. Peng, Deterministic quantum teleportation through fiber channels, Sci. Adv. 4 (10) (2018) 1–7.

[2] M.R. Huo, J.L. Qin, Y.R. Sun, J.L. Cheng, Z.H. Yan, X.J. Jia, Generation of intensity difference squeezed state of light at optical fiber communication wavelength, J. Quantum Opt. 24 (2) (2018) 134–140.

[3] H.J. Kimble, The quantum internet, Nature 453 (2008) 1023–1030.

[4] U. Eismann, A. Bergschneider, F. Sievers, N. Kretzschmar, C. Salomon, F. Chevy, 2.1-watts intracavity-frequency-doubled all-solid-state light source at 671 nm for laser cooling of lithium, Opt. Express 21 (7) (2013) 9091–9102.

[5] L. Winkelmann, O. Puncken, R. Kluzik, C. Veltkamp, P. Kwee, J. Poeld, C. Bogan, B. Willke, M. Frede, J. Neumann, P. Wessels, D. Kracht, Injection-locked single-frequency laser with an output power of 220 W, Appl. Phys. B 102 (3) (2011) 529–538.

[6] B.P. Abbott, R. Abbott, T.D. Abbott, M.R. Abernathy, F. Acernese, et al., Observation of gravitational waves from a binary black hole merger, Phys. Rev. Lett. 116 (6) (2016) 061102–1–061102–16.

[7] P.X. Jin, H.D. Lu, Y.X. Wei, J. Su, K.C. Peng, Single-frequency CW Ti:sapphire laser with intensity noise manipulation and continuous frequency-tuning, Opt. Lett. 42 (1) (2017) 143–146.

[8] R.G. Batchko, D.R. Weise, T. Plettner, G.D. Miller, M.M. Fejer, R.L. Byer, Continuous-wave 532-nm-pumped singly resonant optical parametric oscillator based on periodically poled lithium niobate, Opt. Lett. 23 (3) (1998) 168–170.

[9] N.Y. Kostyukova, A.A. Boyko, V. Badikov, D. Badikov, G. Shevyrdyaeva, V. Panyutin, G.M. Marchev, D.B. Kolker, V. Petrov, Widely tunable in the mid-IR $BaGa_4Se_7$ optical parametric oscillator pumped at 1064 nm, Opt. Lett. 41 (15) (2016) 3667–3670.

[10] M.Z. Xu, Y.R. Guo, J. Su, H.D. Lu, 125 W single-frequency CW Nd:YVO_4 laser based on two-stage dual-end-pumped master-oscillator power amplifiers, Laser Phys. Lett. 16 (2019) 036201.

[11] Y.R. Guo, H.D. Lu, M.Z. Xu, J. Su, K.C. Peng, Investigation about the influence of longitudinal-mode structure of the laser on the relative intensity noise properties, Opt. Express 26 (16) (2018) 21108–21118.

[12] Y.R. Guo, M.Z. Xu, W.N. Peng, J. Su, H.D. Lu, K.C. Peng, Realization of a 101 W single-frequency continuous wave all-solid-state 1064 nm laser by means of mode self-reproduction, Opt. Lett. 43 (24) (2018) 6017–6020.

[13] Q.W. Yin, H.D. Lu, J. Su, K.C. Peng, High power single-frequency and frequency-doubled laser with active compensation for the thermal lens effect of terbium gallium garnet crystal, Opt. Lett. 41 (9) (2016) 2033–2036.

[14] Y.Y. Ma, Y.J. Li, J.X. Feng, K.S. Zhang, High-power stable continuous-wave single-longitudinal-mode Nd:YVO_4 laser at 1342 nm, Opt. Express 26 (2) (2018) 1538–1546.

[15] Y.H. Zheng, Y.J. Wang, C.D. Xie, K.C. Peng, Single-frequency Nd:YVO_4 laser at 671 nm with high-output power of 2.8 W, IEEE J. Quantum Electron. 48 (1) (2012) 67–72.

[16] A.A. Kananovich, V.I. Dashkevich, P.A. Apanasevich, D.H. Zusin, V.A. Orlovich, Eye-safe solid-state quasi-CW Raman laser with millisecond pulse duration, Opt. Commun. 285 (10–11) (2012) 2719–2723.

[17] M. Okida, M. Itoh, T. Yatagai, H. Ogilvy, J. Piper, T. Omatsu, Heat generation in nd doped vanadate crystals with 1.34 μm laser action, Opt. Express 13 (13) (2005) 4909–4915.

[18] L. Fornasiero, S. Kück, T. Jensen, G. Huber, B.H.T. Chai, Excited state absorption and stimulated emission of Nd^{3+} in crystals. Part2: YVO_4, $GdVO_4$, and $Sr_5(PO_4)_3F$, Appl. Phys. B 67 (5) (1998) 549–553.

[19] Y.F. Chen, L.J. Lee, T.M. Huang, C.L. Wang, Study of high-power diode-end-pumped Nd:YVO_4 laser at 1.3 μm: Influence of Auger upconversion, Opt. Commun. 163 (4) (1999) 198–202.

[20] Y.Y. Ma, Y.J. Li, J.X. Feng, K.S. Zhang, Influence of energy-transfer upconversion and excited-state absorption on a high power Nd:YVO_4 laser at 1.34 μm, Opt. Express 26 (9) (2018) 12106–12120.

[21] Q. Shen, X.Y. Cui, M.C. Yan, U. Eismann, T. Yuan, W.Z. Zhang, C.Z. Peng, Y.A. Chen, J.W. Pan, 11-watt single-frequency 1342-nm laser based on multi-segmented Nd:YVO_4 crystal, Opt. Express 27 (22) (2019) 31913–31925.

[22] Y.J. Wang, Y.H. Zheng, Z. Shi, K.C. Peng, High-power single-frequency Nd:YVO_4 green laser by self-compensation of astigmatisms, Laser Phys. Lett. 9 (7) (2012) 506–510.

[23] M.D. Louis, 888 nm Pumping of Nd:YVO_4 for High-power TEM_{00} Lasers (Ph. D. dissertation), Fachbereich Physik, Technische Universität Kaiserslautern, Kaiserslautern, Germany, 2008.

[24] Y.F. Chen, C.C. Liao, Y.P. Lan, S.C. Wang, Determination of the Auger upconversion rate in fiber-coupled diode end-pumped Nd:YAG and Nd:YVO_4 crystals, Appl. Phys. B 70 (4) (2000) 487–490.

[25] Y.F. Chen, Pump-to-mode size ratio dependence of thermal loading in diode-end-pumped solid-state lasers, J. Opt. Soc. Amer. B 17 (11) (2000) 1835–1840.

[26] F. Lenhardt, M. Nittmann, T. Bauer, J. Bartschke, J.A. L'huillier, High-power 888-nm-pumped Nd:YVO_4 1342-nm oscillator operating in the TEM_{00} mode, Appl. Phys. B 96 (4) (2009) 803–807.

[27] Q.W. Yin, H.D. Lu, K.C. Peng, Investigation of the thermal lens effect of the TGG crystal in high-power frequency-doubled laser with single frequency operation, Opt. Express 23 (4) (2015) 4981–4990.

[28] G. Tawy, J. Wang, M.J. Damzen, Pump-induced lensing effects in diode pumped Alexandrite lasers, Opt. Express 27 (24) (2019) 35865–35883.

[29] Z. Zhuo, T. Li, X.M. Li, H.Z. Yang, Investigation of Nd:YVO_4/YVO_4 composite crystal and its laser performance pumped by a fiber coupled diode laser, Opt. Commun. 274 (1) (2007) 176–181.